

Enhancement of second harmonic generation in two-dimensional materials with dual-stopband distributed Bragg reflector

Mengyuan Jia(贾梦源), Jukun Zhan(詹居坤), Tiejun Huang(黄铁军), Jiang Zeng(曾江), Yanan Dai(戴亚南), and Mingyuan Huang(黄明远)

Citation: Chin. Phys. B, 2026, 35 (**8**): 084206. DOI: 10.1088/1674-1056/ae6178
http://cpb.iphy.ac.cn; http://iopscience.iop.org/cpb

What follows is a list of articles you may be interested in

Bistable Goos-Hänchen shift owing to leaky-mode excitation in a slab waveguide with Kerr nonlinear medium

Yuan-Ping Cai(蔡园平), Li Jiang(姜丽), and Ren-Gang Wan(万仁刚)
Chin. Phys. B, 2026, 35 (**4**): 044203. DOI: 10.1088/1674-1056/ae00b3

Mode and orbital angular momentum controlling of nonlocal solitons by anisotropic diffraction

Junying Zhu(朱俊英), Qing Wang(王清), and Jianning Wei(魏健宁)
Chin. Phys. B, 2026, 35 (**4**): 044202. DOI: 10.1088/1674-1056/ae0163

Charge-imbalance-induced second harmonic generation in twisted graphene

Ronghui Luo(罗荣辉), Shiyang Liu(刘诗洋), Xiao Dong(董校), Jianguo Tian(田建国), and Zhibo Liu(刘智波)
Chin. Phys. B, 2026, 35 (**3**): 034201. DOI: 10.1088/1674-1056/ae3557

TaS_2-based saturable absorbers for *Q*-switched fiber laser applications

Qinghua Wang(汪情华), Hao Sun(孙昊), Chenhao Lu(鲁晨浩), Huiran Yang(杨慧苒), and Lu Li(李璐)
Chin. Phys. B, 2025, 34 (**7**): 074209. DOI: 10.1088/1674-1056/addcd7

Real-time observations of the transition dynamics between multiple nonlinear states in a coherently driven Kerr fiber-loop resonator

Yayu Cao(曹亚昱), Heng Dong(董恒), and Xiankun Yao(姚献坤)
Chin. Phys. B, 2025, 34 (**7**): 074206. DOI: 10.1088/1674-1056/adc40a

---

RAPID COMMUNICATION

Enhancement of second harmonic generation in two-dimensional materials with dual-stopband distributed Bragg reflector

Mengyuan Jia(贾梦源)[1], Jukun Zhan(詹居坤)[1], Tiejun Huang(黄铁军)[1], Jiang Zeng(曾江)[2], Yanan Dai(戴亚南)[1], and Mingyuan Huang(黄明远)[1,†]

[1] *Department of Physics, Southern University of Science and Technology, Shenzhen* 518055, *China*

[2] *Nano Fabrication Facilities (NFF), Core Research Facilities, Southern University of Science and Technology, Shenzhen* 518055, *China*

(Received 27 February 2026; revised manuscript received 10 April 2026; accepted manuscript online 20 April 2026)

As a prominent branch of nonlinear optics (NLO), second-harmonic generation (SHG) has been widely studied in fields such as optics, electronics, and materials science. Due to their high conversion efficiency and relaxed phase matching constraints, two-dimensional (2D) materials have become an attractive platform for SHG research. In this work, monolayer $MoSe_2$ was used as the active material, and a dual-stopband distributed Bragg reflector (DBR) structure was fabricated by plasma-enhanced chemical vapor deposition (PECVD) to enhance the SHG efficiency of monolayer $MoSe_2$. The DBR provided substantial enhancement at both the excitation and emission wavelengths. Compared to $MoSe_2$ on a Si substrate, the sample on the DBR exhibited an SHG signal enhancement of over 4000 times. Polarization-dependent measurements showed that the SHG response of $MoSe_2$ on the DBR retained the same polarization dependence as that on the Si substrate. Furthermore, temperature-dependent measurements confirmed that the variation of the SHG signal with temperature followed a consistent trend for $MoSe_2$ on both substrates.

Keywords: nonlinear optics, second-harmonic generation, two-dimensional materials, signal enhancement

PACS: 42.65.–k, 42.65.ky, 78.67.–n

DOI: 10.1088/1674-1056/ae6178 **CSTR:** 32038.14.CPB.ae6178

1. Introduction

In modern optics, nonlinear optics (NLO) plays an important role in areas such as light source fabrication,[1] micro–nano electronics,[2] measurement of physical parameters,[3] and investigation of new material properties.[4] As a typical nonlinear optical process, second-harmonic generation (SHG) is a widely used tool due to its relatively simple mechanism for generation, relaxed generation conditions, high sensitivity to crystal symmetry and electronic structure, and ease of observation. Consequently, SHG has garnered considerable interest in research and applications in material characterization,[3,5] electronic device fabrication,[6] biological sensing,[7] optoelectronic integration,[8] and beyond.

Layered two-dimensional (2D) materials offer inherent advantages for SHG, such as relaxed phase-matching requirements,[9] flexible stacking configurations,[10,11] and ease of integration.[12] However, their atomic-scale thickness, while bringing many advantages, also results in limited efficiency in both excitation absorption and light emission extraction. To address this, several strategies have been developed to enhance SHG in 2D materials, including doping,[2,13,14] strain engineering,[15,16] excitonic resonance,[17] cavity enhancement,[18] plasmonic amplification,[19] and metasurface coupling.[20] Among these techniques, substrate engineering — which enhances SHG by modifying only the underlying substrate without altering the 2D material itself — has gained significant attention. First, it exhibits broad applicability: a substrate optimized for one material can often be adapted to others with minor adjustments while maintaining similar enhancement effects.[21] Second, it demonstrates strong compatibility, allowing the enhanced samples to remain suitable for subsequent studies such as strain tuning,[22] excitonic resonance analysis,[23] and electrode integration.[24] Additionally, the relatively broad bandwidth of substrate-enhanced SHG represents another notable benefit. Within the family of 2D transition metal dichalcogenides (TMDs), $MoSe_2$ exhibits a large second-order nonlinear susceptibility ($\chi^{(2)}$) in odd-numbered layers, with monolayer values reaching the order of 1.7×10^6 pm^2/V.[22] It also benefits from well-established deposition methods, stable crystallographic and chemical properties,[25–27] and distinct spectral features,[28] making it a frequently used model system for SHG studies.

In this work, using monolayer $MoSe_2$ as the SHG-active material, we designed a dual-stopband distributed Bragg reflector (DBR) structure to enhance the electric fields at both the excitation and emission wavelengths simultaneously. The DBR structure was sequentially followed by a spacer layer and a monolayer $MoSe_2$. For this microcavity structure, the

†Corresponding author. E-mail: huangmy@sustech.edu.cn

© 2026 Chinese Physical Society and IOP Publishing Ltd. All rights, including for text and data mining, AI training, and similar technologies, are reserved.

bottom DBR and the top $MoSe_2$/air interface formed reflective boundaries, while the spacer layer and $MoSe_2$ constituted the cavity length. By optimizing the thickness of the spacer layer, we achieved a maximum SHG enhancement exceeding 4000 times compared to the same flake on a Si substrate. Back-reflection measurements[29] confirmed that the enhancement is non-selective to the pump polarization. Furthermore, temperature-dependent measurements showed that the SHG signal from $MoSe_2$ on both substrates increases linearly with temperature at a similar rate, demonstrating the broad applicability of the approach. This study provides a useful reference for the further exploration of SHG materials and device fabrication.

2. Experimental results and discussion

The study was initiated by examining the properties of monolayer $MoSe_2$ on a silicon wafer. Figure 1(a) shows an optical micrograph of mechanically exfoliated monolayer $MoSe_2$ on the bare Si substrate, which serves as a reference for our SHG study. The search for monolayer $MoSe_2$ on a Si wafer was not as smooth as on SiO_2/Si substrate (SiO_2 thickness of about 285 nm), so we adopted a slightly simpler method to simplify this step, as shown in supplementary Fig. S1. Figure 1(b) presents the room-temperature photoluminescence (PL) and differential reflection spectra, both consistent with monolayer behavior[28] (further validation is provided in supplementary Fig. S2). The low-temperature differential reflection spectroscopy measurements in Fig. 1(c) reveal A- and B-exciton peaks in the ranges of 770 nm–790 nm and 675 nm–695 nm, respectively. These results confirm that our SHG excitation wavelength (1033.3 nm, 1.20 eV) avoids direct resonance with these excitonic transitions, enabling a pure optical-field enhancement of SHG without excitonic contributions. Based on previous reports,[30,31] the C-exciton lies above 2.4 eV, which we have also intentionally avoided in our measurements.

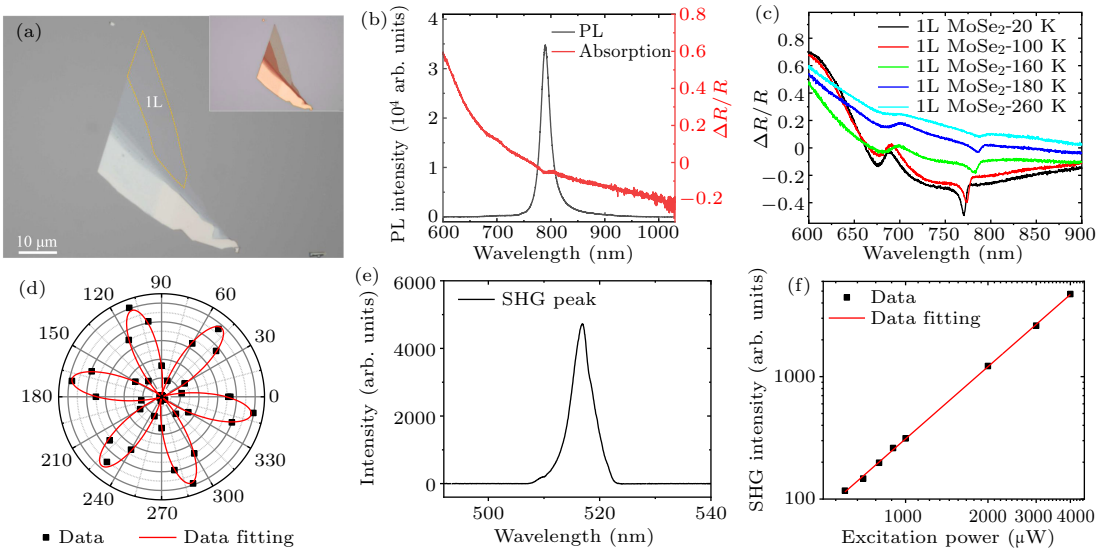


Fig. 1. (a) Optical micrograph of thin $MoSe_2$ films on a Si substrate, with the monolayer $MoSe_2$ area highlighted by orange dashed lines. Inset: The same flake after being transfer onto a 238 nm SiO_2/DBR substrate. (b) Room-temperature PL and differential reflection spectra of the monolayer $MoSe_2$ on Si. (c) Differential reflection spectra of a monolayer $MoSe_2$ sample measured at different temperatures. (d) SHG intensity of the monolayer $MoSe_2$ as a function of the excitation polarization angle. (e) A representative SHG spectrum. (f) SHG intensity of the monolayer $MoSe_2$ as a function of the excitation power. The black square represents the measurement data, and the red line represents the fitted line with a slope of 2.06.

Following the characterization of a monolayer $MoSe_2$ flake, its SHG properties were characterized using the experimental setup illustrated in Fig. S3. An ultrafast laser (Langyantech's YbFemto, 25 MHz repetition rate, 126 fs pulse width) was used with parallel polarizers for excitation and emission. The polarization-dependent SHG response is shown in Fig. 1(d). The data were fitted with the function $\cos^2(3\varphi + \varphi_0)$, where φ is the angle between the laser polarization and the $MoSe_2$ armchair direction, and φ_0 is the initial crystal orientation. The resulting six-lobed pattern reflects the threefold rotational symmetry characteristic of D_{3h} crystals.[32] Figure 1(e) displays a representative SHG spectrum centered at 516.6 nm, with a full width at half maximum (FWHM) of 4.2 nm and a full width at 5% maximum of 12.1 nm. The power-dependent SHG intensity at the polarization angle of maximum signal ($\sim 50°$) is shown in Fig. 1(f). A linear fit in the double-logarithmic plot yields a slope of 2.06, confirming the quadratic dependence of SHG intensity on pump power.[22]

Since the SHG intensity depends on the product of the local fields at both the excitation wave and the emission wave, simultaneous enhancement of these two fields can lead to a maximized nonlinear response. Guided by this principle, we designed a dual-stopband DBR using the transfer matrix method

(TMM):

$$\begin{pmatrix} \cos\delta_j & \frac{\mathrm{i}}{N_j}\sin\delta_j \\ \mathrm{i}N_j\sin\delta_j & \cos\delta_j \end{pmatrix}. \tag{1}$$

where δ_j is the phase shift generated by the beam passing through the jth layer film, with $\delta_j = (2\pi/\lambda)N_j d_j$, N_j is the complex refractive index of the jth layer film material, $N_j = n_j - \mathrm{i}k_j$, n_j is the refractive index of the jth material, k_j is the absorption coefficient of the jth material, and d_j is the geometric thickness of the jth layer film. Based on the existing experimental conditions, we used SiN_x and SiO_2 as dielectric materials to construct the dual-stopband DBR. The refractive index and absorption coefficient of these materials were measured by an ellipsometer as shown in Figs. 2(b) and 2(c), with a measurement accuracy of 1 nm. Considering that the refractive index and absorption coefficient of SiN_x vary greatly with wavelength, the refractive index (absorption coefficient) at the emission and absorption wavelengths changes by 4.9% (400%). Designing a DBR with a fixed refractive index value (absorption coefficient) can easily lead to errors, so we established the functional relationship between refractive index and absorption coefficient and incident wavelength using an interpolation method in the range of 400–1100 nm, and simulated the reflectivity and electric field distribution of the dual-stopband DBR. As illustrated in Fig. 2(a), the device is composed of a 12.5-pair DBR (including SiN_x as the high-index layer and SiO_2 as the low-index layer, with thicknesses of $d_H = 59.6$ nm and $d_L = 260.2$ nm, respectively) and topped with a SiO_2 spacer layer. The calculated reflectance spectrum (without the SiO_2 spacer layer, Fig. 2(d), red curve) confirms that this structure provides high-reflectance stopbands centered at both the excitation wavelength λ_0 and its half ($\lambda_0/2$, the emission wavelength), enabling the desired dual-wavelength resonance.

The DBR was fabricated via plasma-enhanced chemical vapor deposition (PECVD; Oxford Instruments PlasmaPro 80). The measured reflectance spectrum (Fig. 2(d), black curve) shows reflectivity of 98.5% and 97.6% at the excitation and emission wavelengths, respectively, in good agreement with simulations. In this regard, a relatively clean coating chamber environment and a prolonged warm-up process are unavoidable. Although slight deviations in the central stopband positions are observed, the 95%-reflectance bandwidths are 131 nm (excitation) and 51 nm (emission), ensuring stable operation within the stopbands.

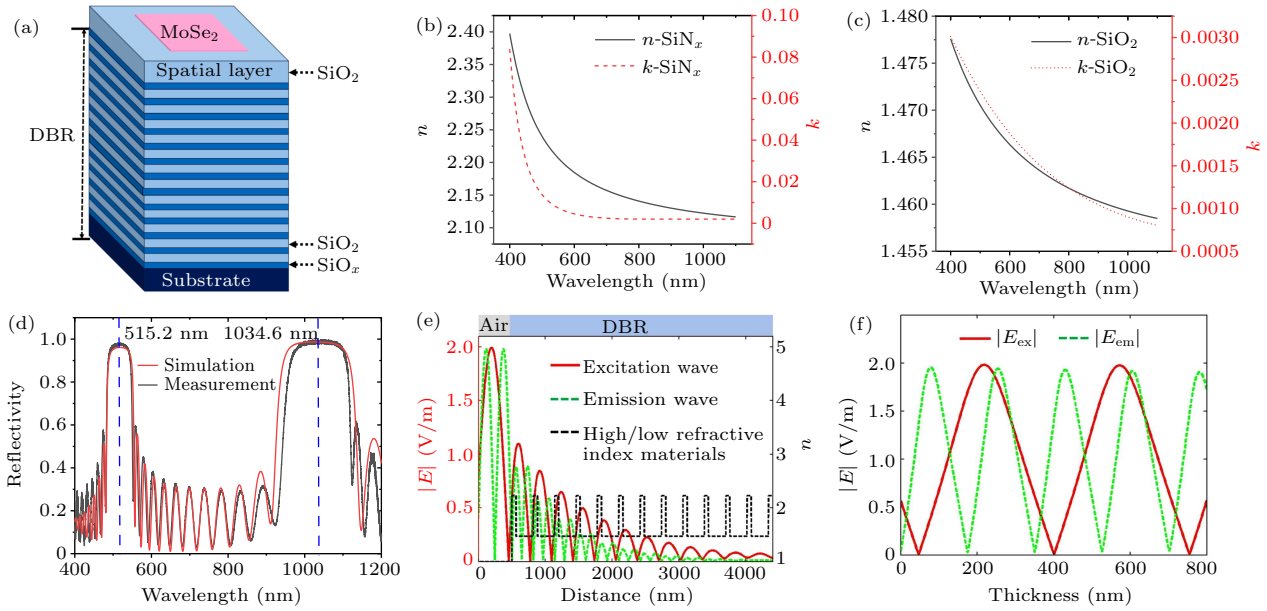


Fig. 2. (a) Schematic illustration of the dual-stopband DBR device. (b) and (c) Refractive index (n) and extinction coefficient (k) of (b) SiN_x and (c) SiO_2 measured by spectroscopic ellipsometry. (d) Calculated (red curve) and experimentally measured (black curve) reflectance spectra of the dual-stopband DBR. (e) Calculated electric field distribution across the dual-stopband DBR structure. The black dashed curve indicates the material stratification according to the refractive index (right y-axis). The red solid and green dashed curves show the field distributions for the excitation wave and the emission wave, respectively (left y-axis). (f) Electric field intensities at excitation (red solid curve) and emission (green dashed curve) wavelengths as a function of the SiO_2 spacer thickness.

To estimate the SHG enhancement effect, the electric field localization on the DBR surface was analyzed under a normalized incident field of 1 V/m. The maximum field amplitudes at the excitation and emission wavelengths are approximately 1.99 V/m and 1.98 V/m, respectively (Fig. 2(e)). Unfortunately, the field maxima for the two wavelengths are not right on the surface of the DBR or spatially coincident, which is the same as the single stopband DBR made of the same material (as shown in supplementary Fig. S4). To maximize SHG intensity, we simulated the electric field distribution as a function of SiO_2 spacer thickness. The complex refractive indices of monolayer $MoSe_2$ were set to 4.5 (at 1033.3 nm) and 5.6–2.6i (at 516.7 nm).[33] Within the calculation range of 800 nm spacer layer thickness, the excitation field exhibits two

peaks of 1.98 V/m and 1.975 V/m at thicknesses of 218 nm and 572 nm, while the emission field exhibits four peaks of 1.95 V/m, 1.94 V/m, 1.93 V/m, and 1.92 V/m at thicknesses of 78 nm, 254 nm, 430 nm, and 606 nm (as shown in Fig. 2(f)). The slight decrease in peak electric fields of both the excitation and emission fields with increasing spatial layer thickness is attributed to the non-zero extinction coefficients of the SiO_2 spacer layer at both the excitation and emission wavelengths (as illustrated in Fig. 2(c)). Based on these results, we hypothesized that the maximum combined effect of excitation and emission fields would be achieved at a spacer thickness slightly greater than 218 nm. Therefore, we fabricated DBRs with spacer thicknesses of 218 nm, 228 nm, 238 nm, 248 nm, 258 nm, and an additional 20 nm. Monolayer $MoSe_2$ flakes were transferred from Si onto these DBRs to experimentally determine the optimal thickness for SHG enhancement (sample images in Fig. S5).

Post-transfer SHG measurements are summarized in Fig. 3(a). For clarity, signals from $MoSe_2$ on Si and on the 20 nm SiO_2/DBR are magnified by 400×, and the peak positions of $MoSe_2$ on 218 nm, 228 nm, 248 nm, and 258 nm SiO_2/DBR are horizontally offset. Compared to the Si reference, samples on DBRs with spacer thicknesses of 218 nm, 228 nm, 238 nm, 248 nm, and 258 nm exhibited SHG enhancements by factors of 2973, 4031, 4140, 3883, and 2821, respectively, with no change in spectral shape. In contrast, the 20 nm spacer sample showed suppression, with SHG intensity only 0.77 times that on Si, indicating that the SiO_2 spacer thickness can lead not only to significant enhancement but also to minor suppression.

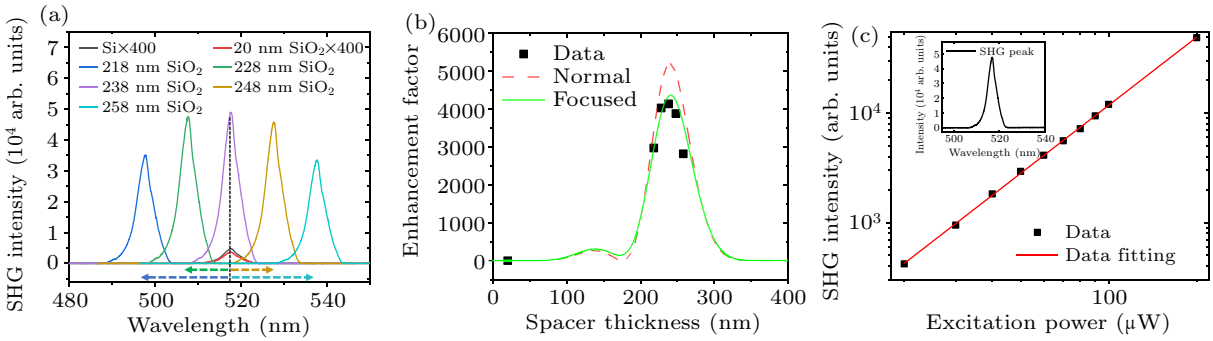


Fig. 3. (a) SHG signal intensity from monolayer $MoSe_2$ on a Si substrate and on SiO_2/DBR structures with different spacer thicknesses. For the convenience of intensity comparison, the signals emitted by single-layer $MoSe_2$ samples with spatial layer thicknesses of 218 nm, 228 nm, 248 nm and 258 nm were shifted on the x-axis, as indicated by the colored dashed arrows in the figure. (b) Enhancement factor of the SiO_2/DBR as a function of the spacer thickness. Black squares represent the experimental data, the red dashed curve represents the fitting result of normal incidence, while the green solid curve represents the fitting result of oblique incidence. (c) Power-dependent SHG intensity of monolayer $MoSe_2$ on the 238 nm SiO_2/DBR, with a linear fit slope of 2.07. Inset: a representative SHG spectrum.

We employed the model developed by Lien *et al.*,[34] and the final emitted SHG intensity, I_{SHG}, is given by

$$I_{SHG} = \int_0^d |E_{ex}(x)|^4 |E_{em}(x)|^2 \, dx, \tag{2}$$

where d is the thickness of the monolayer $MoSe_2$, taken as 0.65 nm,[35] and $E_{ex}(x)$ and $E_{em}(x)$ represent the electric field amplitudes of the excitation and emission waves within the monolayer $MoSe_2$, respectively. In addition, two other factors are considered. Firstly, the dry transfer process using poly (methyl ethyl carbonate) as an adhesive reduced the SHG intensity of monolayer $MoSe_2$ by a factor of 1.2–1.4, though no crystal fragmentation was observed. The main changes brought by the dry transfer process to the material are strain effects and the cleanliness of the material surface. Strain can lead to a decrease in the inherent SHG of the material, while cleanliness leads to a decrease in the ambient light field of the material, weakening the gain effect of the device on SHG. Due to the fact that strain not only changes the inherent SHG intensity, but also alters the symmetry of the lattice, the six-petal symmetry exhibited by the SHG of the transferred sample indicates that the effect of strain is not significant.[3,36] The PL of the transferred samples did not show significant changes, indicating that the degree of contamination on the material surface was not significant (supplementary materials, Section 6). The influence of strain is minimal and the material surface is difficult to distinguish, so the statistical data transmitted from multiple samples are the only choice for us to understand the degree of SHG signal reduction, as shown in supplementary materials, Section 6. Secondly, considering the use of an objective lens with NA of 0.55 to focus the laser beam, we calculated the SHG by accounting for oblique incidence effects (supplementary Section 7). After incorporating these two factors, the results show excellent agreement with experimental data after normalization to the Si substrate case (Fig. 3(b)). We measured the SHG signal intensity and excitation power of single-layer $MoSe_2$ on 238 nm SiO_2/DBR at room temperature, as shown in Fig. 3(c). The fitted line slope of the double logarithmic plot of the two is 2.07, indicating that the excitation and emission waves of single-layer $MoSe_2$ on 238 nm SiO_2/DBR still maintain a quadratic relationship.

Furthermore, we explored the performance of the dual-stopband DBR at low temperatures, and the temperature-

dependent SHG measurements were conducted on the same $MoSe_2$ flake transferred onto both a Si substrate and the optimal 238 nm SiO_2/DBR (Figs. 4(a) and 4(b)). The SHG intensity increases linearly with temperature on both substrates, with fitted slopes of 1.78×10^{-3} K^{-1} (Si) and 1.56×10^{-3} K^{-1} (238 nm SiO_2/DBR). This overall temperature-induced increase in SHG is consistent with previous reports.[37] The slight difference in the slopes (12%) is attributed to different substrates. As described by Khan *et al.*,[37] the $\chi^{(2)}$ of monolayer TMDs decreases with an increasing in-plane lattice constant but increases with an increasing vertical lattice constant. Monolayer $MoSe_2$, possessing a positive in-plane Poisson's ratio and a negative out-of-plane Poisson's ratio,[38,39] exhibits a simultaneous increase in both its in-plane and out-of-plane lattice constants with rising temperature. However, the contribution from the increase in the out-of-plane lattice constant to the SHG enhancement outweighs the reduction caused by the in-plane lattice expansion. Consequently, the net $\chi^{(2)}$ of monolayer $MoSe_2$ increases with temperature. Within the measured temperature range of 7 K to 300 K, the relationship between the thermal expansion coefficients (α) is $\alpha(MoSe_2) > \alpha(Si) > \alpha(SiO_2)$ (at 300 K, $\alpha(MoSe_2)\approx 8\times10^{-6}$ K^{-1}, $\alpha(Si)\approx 3\times10^{-6}$ K^{-1}, $\alpha(SiO_2)\approx 0.4\times10^{-6}$ K^{-1}).[40–43] This means that as temperature increases, the thermal expansion of the $MoSe_2$ lattice is constrained by the substrate. Because the Si substrate has a higher thermal expansion coefficient than the SiO_2/DBR substrate, the relative thermal expansion of $MoSe_2$ on Si is greater than that on the 238 nm SiO_2/DBR. This leads to a more pronounced temperature-dependent increase in SHG intensity for $MoSe_2$ on Si, resulting in a higher efficiency gain. Furthermore, differences in sample preparation and substrate morphology contribute to the observed slope difference. The $MoSe_2$ on Si was prepared by mechanical exfoliation, while the sample on SiO_2/DBR was prepared by dry transfer. Compared with dry transfer, $MoSe_2$ obtained by mechanical exfoliation method adheres more tightly to the substrate, and dry transfer can release some stress from the sample, which is evidence.[22] Additionally, the surface of the PECVD-deposited SiO_2 is slightly less smooth than that of the Si wafer, which further reduces the adhesion between $MoSe_2$ and the 238 nm SiO_2/DBR substrate. This lower adhesion diminishes the substrate's damping effect on the thermal expansion of the monolayer $MoSe_2$ compared to the Si case. Although there is a significant difference in the thermal expansion coefficients between the Si and SiO_2/DBR substrates, the reduced adhesion on SiO_2/DBR mitigates the difference in the rate of SHG increase for monolayer $MoSe_2$ on the two substrates. A key operational advantage of the DBR substrate is that its high enhancement efficiency enables low-power operation, thereby avoiding the strong parasitic SHG background from the Si substrate itself (arising from surface symmetry breaking[44]). The results of this measurement can be seen in Fig. S14. In addition, the polarization-resolved SHG maintained its characteristic sixfold symmetry during the process of increasing from low temperature to 270 K (Figs. 4(e) and 4(f)), and the power-dependent response confirmed the quadratic relationship (Fig. 4(c) slope = 2.04, Fig. 4(d) slope = 2.07).

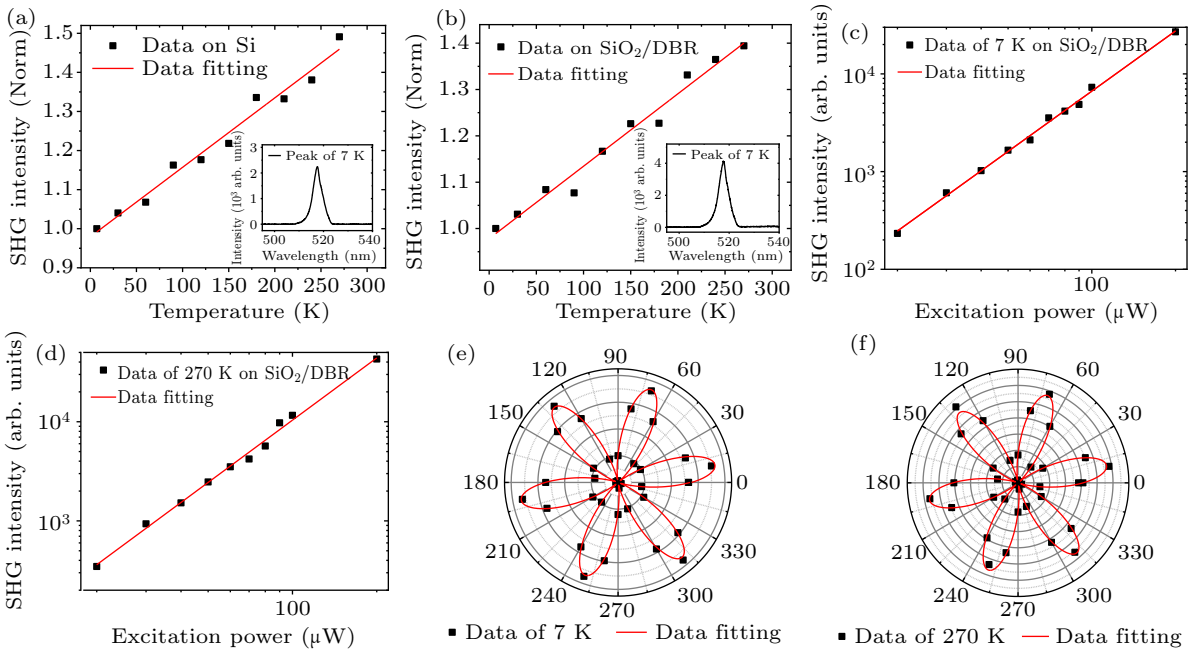


Fig. 4. SHG intensity of $MoSe_2$ as a function of temperature on (a) Si and (b) 238 nm SiO_2/DBR substrates, with linear-fit slopes of 1.78×10^{-3} K^{-1} and 1.56×10^{-3} K^{-1}, respectively. All data were normalized against the 7 K measurement. Inset: SHG spectrum measured at 7 K. (c) and (d) SHG intensity of monolayer $MoSe_2$ on the 238 nm SiO_2/DBR substrate at 7 K and 270 K as a function of the excitation power. The red line in (c) and (d) represents a linear fit with a slope of 2.05 and 2.07, respectively. (e) and (f) SHG intensity of monolayer $MoSe_2$ on the 238 nm SiO_2/DBR substrate at 7 K and 270 K as a function of the excitation polarization angle.

3. Conclusion and perspectives

In summary, we have demonstrated a more than 4000-fold enhancement of SHG in monolayer $MoSe_2$ by integrating it with a dual-stopband DBR. The relationship between the measured SHG intensity and the pump power confirms a clear quadratic dependence for $MoSe_2$ on both the Si substrate and the SiO_2/DBR. Polarization-dependent measurements reveal a six-lobed pattern for $MoSe_2$ on the SiO_2/DBR, indicating that the material retains the threefold rotational symmetry characteristic of its D_{3h} crystal structure. Furthermore, in variable-temperature measurements, the stable dual-stopband DBR enables $MoSe_2$ to exhibit a temperature-dependent response similar to that on a Si substrate. This work provides valuable insights for studying SHG in 2D materials and offers a practical strategy for significantly enhancing the SHG intensity.

Acknowledgements

Project supported by the National Natural Science Foundation of China (Grant Nos. 12074165, 12374223, and 92477108) and Shenzhen Science and Technology Program (Grant No. 20231117151322001).

References

[1] Keller U 2003 *Nature* **424** 831
[2] Seyler K L, Schaibley J R, Gong P, Rivera P, Jones A M, Wu S, Yan J, Mandrus D G, Yao W and Xu X 2015 *Nat. Nanotech.* **10** 407
[3] Liang J, Zhang J, Li Z, Hong H, Wang J, Zhang Z, Zhou X, Qiao R, Xu J, Gao P, Liu Z, Liu Z, Sun Z, Meng S, Liu K and Yu D 2017 *Nano Lett.* **17** 7539
[4] Abdelwahab I, Tilmann B, Zhao X, Verzhbitskiy I, Berté R, Eda G, Wilson W L, Grinblat G, Menezes L S, Loh K P and Maier S A 2023 *Adv. Opt. Mater.* **11** 2202833
[5] Sun Z, Zhang Y, Qian J, Qiao R, Li X, Wang Z, Zheng C, Liu K, Cao T, Liu W T and Wu S 2022 *Adv. Opt. Mater.* **10** 2201183
[6] Zuo Y, Yu W, Liu C, Cheng X, Qiao R, Liang J, Zhou X, Wang J, Wu M, Zhao Y, Gao P, Wu S, Sun Z, Liu K, Bai X and Liu Z 2020 *Nat. Nanotech.* **15** 987
[7] Tran R J, Sly K L and Conboy J C 2017 *Annu. Rev. Anal. Chem.* **10** 387
[8] Zhu C Y, Zhang Z, Qin J K, Wang Z, Wang C, Miao P, Liu Y, Huang P Y, Zhang Y, Xu K, Zhen L, Chai Y and Xu C Y 2023 *Nat. Commun.* **14** 2521
[9] Zhao M, Ye Z, Suzuki R, Ye Y, Zhu H, Xiao J, Wang Y, Iwasa Y and Zhang X 2016 *Light* **5** e16131
[10] Zhang X Q, Lin C H, Tseng Y W, Huang K H and Lee Y H 2015 *Nano Lett.* **15** 410
[11] Hsu W T, Zhao Z A, Li L J, Chen C H, Chiu M H, Chang P S, Chou Y C and Chang W H 2014 *ACS Nano* **8** 2951
[12] Shi J, He X, Chen W, Li Y, Kang M, Cai Y and Xu H 2022 *Nano Lett.* **22** 688
[13] Le C T, Clark D J, Ullah F, Jang J I, Senthilkumar V, Sim Y, Seong M J, Chung K H, Kim J W, Park S, Rhim S H, Kim G and Kim Y S 2017 *ACS Photonics* **4** 38
[14] Luo R, Liu S, Dong X, Tian J and Liu Z 2026 *Chin. Phys. B* **35** 034201
[15] Tan J, Shi X, Lu K, Joo H J, Kim Y, Chen M, Zhang L, Tan C S, Lim K Y, Quek E and Nam D 2023 *Opt. Lett.* **48** 4269
[16] Chen H, Li S Q, Wu Y, Bao X, Lei Z, Liu H, Xie Y, Gao J, Chen Y and Yan X 2025 *Chin. Phys. B* **34** 084206
[17] Wang G, Marie X, Gerber I, Amand T, Lagarde D, Bouet L, Vidal M, Balocchi A and Urbaszek B 2015 *Phys. Rev. Lett.* **114** 097403
[18] Shi J, Wu X, Wu K, Zhang S, Sui X, Du W, Yue S, Liang Y, Jiang C, Wang Z, Wang W, Liu L, Wu B, Zhang Q, Huang Y, Qiu C W and Liu X 2022 *ACS Nano* **16** 13933
[19] Zhang S, Li G C, Chen Y, Zhu X, Liu S D, Lei D Y and Duan H 2016 *ACS Nano* **10** 11105
[20] Spreyer F, Ruppert C, Georgi P and Zentgraf T 2021 *ACS Nano* **15** 16719
[21] Guo X, Huang M, Gu Y and Yu Y 2025 *Opt. Express* **33** 36597
[22] Puri S, Patel S, Cabellos J L, Rosas-Hernandez L E, Reynolds K, Churchill H O H, Barraza-Lopez S, Mendoza B S and Nakamura H 2024 *Nano Lett.* **24** 13061
[23] Shi J, Liang W Y, Raja S S, Sang Y, Zhang X Q, Chen C A, Wang Y, Yang X, Lee Y H, Ahn H and Gwo S 2018 *Laser Photonics Rev.* **12** 1800188
[24] An Y Q, Rowe J E, Dougherty D B, Lee J U and Diebold A C 2014 *Phys. Rev. B* **89** 115310
[25] Wang Q H, Kalantar-Zadeh K, Kis A, Coleman J N and Strano M S 2012 *Nat. Nanotech.* **7** 699
[26] Peng Y, Meng Z, Zhong C, Lu J, Yu W, Jia Y B and Qian Y 2001 *Chem. Lett.* **30** 772
[27] Matte H S S R, Plowman B, Datta R and Rao C N R 2011 *Dalton Trans.* **40** 10322
[28] Ross J S, Wu S, Yu H, Ghimire N J, Jones A M, Aivazian G, Yan J, Mandrus D G, Xiao D, Yao W and Xu X 2013 *Nat. Commun.* **4** 1474
[29] Guo Q, Qi X Z, Zhang L, Gao M, Hu S, Zhou W, Zang W, Zhao X, Wang J, Yan B, Xu M, Wu Y K, Eda G, Xiao Z, Yang S A, Gou H, Feng Y P, Guo G C, Zhou W, Ren X F, Qiu C W, Pennycook S J and Wee A T S 2023 *Nature* **613** 53
[30] Kikuchi Y, Miyauchi Y, Takaoka R, Suzuki T, Tanaka M and Ohno S 2019 *Phys. Rev. B* **100** 075301
[31] Yao K, Yanev E, Chuang H J, Rosenberger M R, Xu X, Darlington T, McCreary K M, Hanbicki A T, Watanabe K, Taniguchi T, Jonker B T, Zhu X, Basov D N, Hone J C and Schuck P J 2020 *ACS Nano* **14** 708
[32] Wang Y, Xiao J, Yang S, Wang Y and Zhang X 2019 *Opt. Mater. Express* **9** 1136
[33] Kim T J, Park H G, Le V L, Nguyen H T, Nguyen X A and Kim Y D 2019 *AIP Adv.* **9** 125132
[34] Lien D H, Kang J S, Amani M, Chen K, Tosun M, Wang H P, Roy T, Eggleston M S, Wu M C, Dubey M, Lee S C, He J H and Javey A 2015 *Nano Lett.* **15** 1356
[35] Lundt N, Maryński A, Cherotchenko E, Pant A, Fan X, Tongay S, Sęk G, Kavokin A V, Höfling S and Schneider C 2017 *2D Mater.* **4** 015116
[36] Mennel L, Paur M and Mueller T 2019 *APL Photonics* **4** 034404
[37] Khan A R, Liu B, Zhang L, Zhu Y, He X, Zhang L, Lü T and Lu Y 2020 *Adv. Opt. Mater.* **8** 2000441
[38] Yu L, Yan Q and Ruzsinszky A 2017 *Nat. Commun.* **8** 15224
[39] Zhu Y, Cao X, Tan Y, Wang Y, Hu J, Li B and Cheng Z 2023 *Coatings* **13** 283
[40] Xu C H, Wang C Z, Chan C T and Ho K M 1991 *Phys. Rev. B* **43** 5024
[41] Middelmann T, Walkov A, Bartl G and Schödel R 2015 *Phys. Rev. B* **92** 174113
[42] Rego G 2023 *Sensors* **23** 6023
[43] Sevik C 2014 *Phys. Rev. B* **89** 035422
[44] Jun B, White Y V, Schrimpf R D, Fleetwood D M, Brunier F, Bresson N, Cristoloveanu S and Tolk N H 2004 *Appl. Phys. Lett.* **85** 3095